ARTICLE

Magnetic resonance fingerprinting

Dan Ma[1], Vikas Gulani[1,2], Nicole Seiberlich[1], Kecheng Liu[3], Jeffrey L. Sunshine[2], Jeffrey L. Duerk[1,2] & Mark A. Griswold[1,2]

Magnetic resonance is an exceptionally powerful and versatile measurement technique. The basic structure of a magnetic resonance experiment has remained largely unchanged for almost 50 years, being mainly restricted to the qualitative probing of only a limited set of the properties that can in principle be accessed by this technique. Here we introduce an approach to data acquisition, post-processing and visualization—which we term 'magnetic resonance fingerprinting' (MRF)—that permits the simultaneous non-invasive quantification of multiple important properties of a material or tissue. MRF thus provides an alternative way to quantitatively detect and analyse complex changes that can represent physical alterations of a substance or early indicators of disease. MRF can also be used to identify the presence of a specific target material or tissue, which will increase the sensitivity, specificity and speed of a magnetic resonance study, and potentially lead to new diagnostic testing methodologies. When paired with an appropriate pattern-recognition algorithm, MRF inherently suppresses measurement errors and can thus improve measurement accuracy.

Magnetic resonance techniques such as NMR spectroscopy and magnetic resonance imaging (MRI) are widely used throughout physics, biology and medicine because of their ability to generate detailed information about numerous important material or tissue properties, including those reflective of many common disease states[1–4]. However, in practice magnetic resonance acquisitions are often restricted to a qualitative or 'weighted' measurement of a limited set of these properties; the magnetic resonance signal intensity is almost never quantitative by itself. The same material can have different intensities in different data sets depending on many factors, including the type and set-up of the scanner, the detectors used, and so on. Because of this, the quantitative analysis of magnetic resonance results typically focuses on differences between spectral peaks, spatial locations or different points in time. Even in clinical MRI today, a tissue or material is typically referred to as being 'hyperintense' or 'hypo-intense' compared to another area, which may not provide a quantitative indication of the severity of the differences, and may have reduced sensitivity to global changes. Thus robust, fully quantitative multiparametric acquisition has long been the goal of research in magnetic resonance[5–8]. However, the quantitative methods developed to date typically provide information on a single parameter at a time, require significant scan time, and are often highly sensitive to system imperfections. Simultaneous, multiparametric measurements are almost always impractical owing to scan time limits and a high sensitivity to the measurement set-up and experimental conditions. Thus purely qualitative magnetic resonance measurements remain the standard today, particularly in clinical MRI.

Here we introduce a novel approach, namely MRF, that may overcome these constraints by taking a completely different approach to data acquisition, post-processing and visualization. Instead of using a repeated, serial acquisition of data for the characterization of individual parameters of interest, MRF uses a pseudorandomized acquisition that causes the signals from different materials or tissues to have a unique signal evolution or 'fingerprint' that is simultaneously a function of the multiple material properties under investigation. The processing after acquisition involves a pattern recognition algorithm to match the fingerprints to a predefined dictionary of predicted signal evolutions. These can then be translated into quantitative maps of the magnetic parameters of interest.

MRF is related to the concept of compressed sensing[9–12], and shares many of its predicted benefits. For example, preliminary results show that MRF could acquire fully quantitative results in a time comparable to a traditional qualitative magnetic resonance scan, without the high sensitivity to measurement errors found in many other fast methods. Most importantly, MRF has the potential to quantitatively examine many magnetic resonance parameters simultaneously given enough scan time, whereas current magnetic resonance techniques can only examine a limited set of parameters at once. Thus MRF opens the door to computer-aided multiparametric magnetic resonance analyses, similar to genomic or proteomic analyses, that could detect important but complex changes across a large number of magnetic resonance parameters simultaneously. When an appropriate pattern recognition algorithm is used, MRF also provides a new and more robust behaviour in the presence of noise or other acquisition errors that may lead to the near complete suppression of deleterious effects stemming from these factors. Although we focus on demonstrating the feasibility for MRI in this study, it is rather straightforward to translate these results to other magnetic resonance fields, such as multiparametric NMR spectroscopy, dynamic contrast enhanced MRI and dynamic susceptibility contrast MRI[13].

Generation and recognition of MRF signals

The key assumption underlying the MRF concept is that unique signal evolutions, or fingerprints, can be generated for different materials or tissues using an appropriate acquisition scheme. Here we demonstrate that this is possible through the continuous variation of the acquisition parameters throughout the data collection. Variations in the pulse sequence parameters during acquisition have been used previously in MRI and magnetic resonance spectroscopy to reduce the signal oscillations[14] and to improve the spectral response[15–17]. However, these variations were primarily used in a preparation phase or to make the signal more constant. Randomized sampling patterns have also been used previously to aid in the separation of spatiotemporal signals in moving objects or substances with different resonance frequencies[18–20]. Here we demonstrate that temporal and spatial incoherence required in MRF can be achieved by varying acquisition parameters—such as the flip angle and phase of radio frequency pulses, the repetition time, echo time and sampling patterns—in a pseudorandom manner.

[1]Department of Biomedical Engineering, Case Western Reserve University, 10900 Euclid Avenue, Cleveland, Ohio 44106, USA. [2]Department of Radiology, Case Western Reserve University and University Hospitals of Cleveland, 11100 Euclid Avenue, Cleveland, Ohio 44106, USA. [3]Siemens Healthcare USA, 51 Valley Stream Parkway, Malvern, Pennsylvania 19355, USA.

After the data are acquired, the separation of the signal into different material or tissue types can be achieved through pattern recognition. In its simplest form, this process is analogous to matching a person's real fingerprint to a database: once a match is made, a host of additional information about the person, such as name, address and phone number, can be obtained simultaneously once the fingerprint sample is identified. In MRF, this pattern recognition can take place through many means. In the current implementation, we construct a dictionary that contains signal evolutions from all foreseeable combinations of materials and system-related parameters—for example, the longitudinal relaxation time, T_1, the transverse relaxation time, T_2 and off-resonance frequency are included in this study. Other properties could also be measured, such as diffusion and magnetization transfer using the well-established Bloch equation formalism of magnetic resonance [21,22]. Once this dictionary of possible signal evolutions is generated, a matching or pattern recognition algorithm [23,24] is then used to select a signal vector or a weighted set of signal vectors from the dictionary that best correspond to the observed signal evolution. All the parameters that were used to build this signal vector in the dictionary can then be retrieved simultaneously. At present, the calculation of a complete dictionary containing the realistic range of T_1, T_2 and off-resonance frequency requires only a few minutes on a modern desktop computer.

It should be noted that there are near-infinite possibilities for MRF-compatible pulse sequences. Other magnetic resonance parameters of interest can be investigated by identifying pulse sequence components that impart differential sensitivity to the parameters of interest. Moreover, different components can be varied simultaneously, adding the potential for a highly efficient experimental design that allows almost any material characteristic visible using magnetic resonance to be analysed in a quantitative way using MRF.

Validation of the concept

For a proof-of-principle implementation, an MRF acquisition based on an inversion-recovery balanced steady state free-precession (IR-bSSFP) sequence was used (Fig. 1a). This choice of this basic pulse sequence was based on the extensive existing knowledge about IR-bSSFP signal evolution, and its sensitivity to T_1, T_2 and off-resonance frequency [25]. After each radio-frequency pulse, one interleaf of a variable density spiral (VDS) read out [26] was acquired, as shown in Fig. 1b. Such a VDS trajectory has been used in fast imaging [27] and for the reduction of undersampling errors [28]. Two MRF acquisition patterns with randomized flip angle and repetition time were used as shown in

Fig. 1c and d in separate scans to demonstrate the flexibility of the choice of the acquisition parameters.

Figure 2a and b show the simulated signal evolution curves that would be expected from four commonly encountered tissues of the brain (fat, white matter, grey matter and cerebrospinal fluid) using the schematic implementation shown in Fig. 1c and d, respectively. Each tissue type has characteristic T_1 and T_2 values and thus each signal evolution has a different shape, which confirms that it is possible to satisfy this fundamental assumption in MRF. Note also that the signal levels in these evolutions represent a large fraction of the equilibrium magnetization (which is normalized to one in these figures.) Conventional spoiled steady-state sequences typically generate signal levels corresponding to 1–10% of the equilibrium magnetization. Figure 2c and d show an acquired signal evolution curve from fully sampled experiments on manufactured agar 'phantoms' and its match to the dictionary by using the acquisition pattern shown in Fig. 1c and d, along with the recovered T_1, T_2, proton density (M_0) and off-resonance frequency values. MRF was able to match the signal to the corresponding dictionary entry and obtain the same T_1 and T_2 values from both sequence patterns. A video of the signal evolution from a fully sampled *in vivo* scan is available (Supplementary Video 1), demonstrating the oscillating nature of the MRF signal observed *in vivo*.

Accelerated MRF acquisitions

In addition to simultaneously quantifying multiple parameters, the error tolerance of MRF can be significantly better than that of conventional MRI. Because MRF is based on pattern recognition in a setting where the form of all predicted signal evolutions is known, MRF should be less sensitive to errors during the measurement. This is similar to conventional fingerprint recognition techniques, which often contend with smudges and partial fingerprint information. In particular, the interaction of the temporal and spatial incoherence possible in MRF provides new opportunities to accelerate image acquisition through rejection of spatial undersampling errors. In order to test the limits of this acceleration, the same MRF sequence as shown in Fig. 1a–c was modified to use only one spiral readout in each acquisition block. Therefore, the data collected are only 1/48th of the normally required data at each time point, resulting in a total acquisition time of 12.3 s, corresponding to 1,000 sampled time points. (See Fig. 3a and Supplementary Video 2.) The signal evolutions from all 1,000 undersampled time points were used directly to match one entry from the dictionary to quantify T_1, T_2, M_0 and
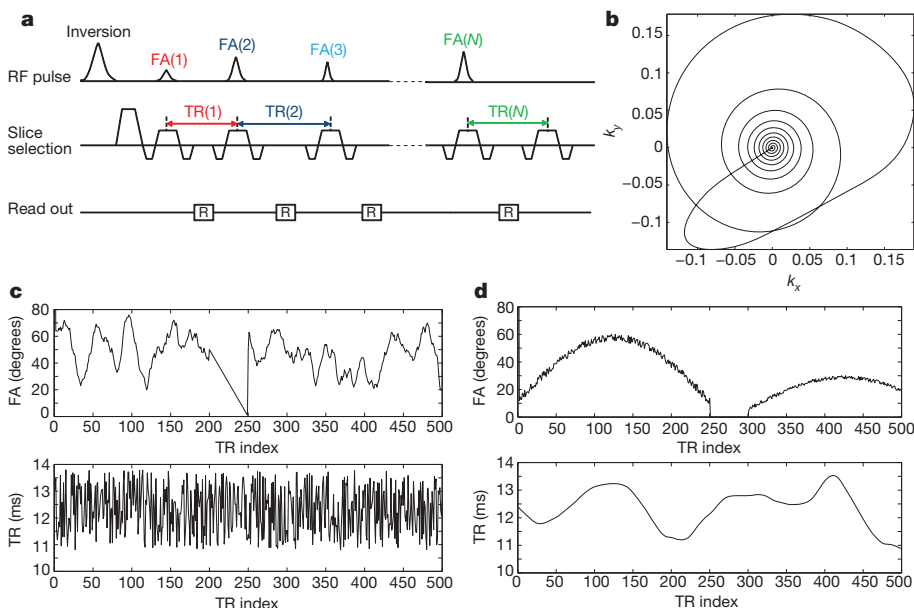

Figure 1 | MRF sequence pattern. a, Acquisition sequence diagram. In each subsequent acquisition block, identified by a repetition time index (TR index; TR(1)...TR(N)), various sequence components are varied in a pseudorandom pattern. FA, flip angle. **b,** Here, one variable density spiral trajectory was used per repetition time. The Fourier coefficients sampled by the variable density spiral trajectory (given by the coordinates k_x and k_y) are rotated from one repetition time to the next. **c, d,** Examples of the first 500 points of flip angle and repetition time patterns that were used in this study.
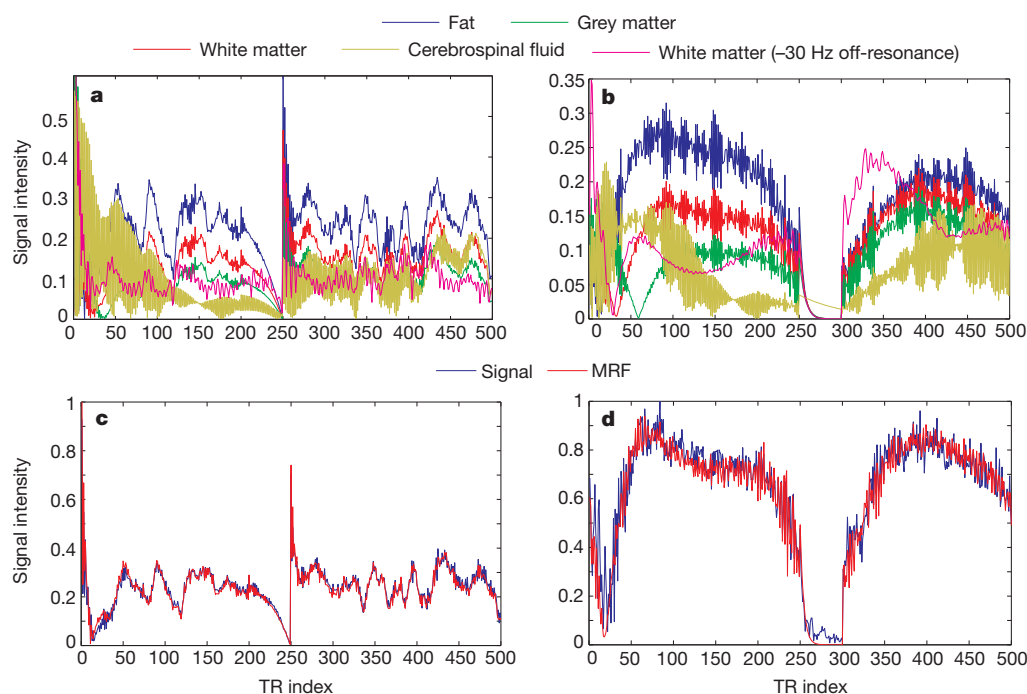
Figure 2 | Signal properties and matching results from phantom study. a, b, Simulated signal evolution curves corresponding to four normal brain tissues using the sequence patterns in Fig. 1c and d, respectively, as a fraction of the equilibrium magnetization. The curve from white matter with off-resonance is also plotted. **c, d,** Measured signal evolutions from one of eight phantoms using different sequence patterns and their dictionary match. The estimated T_1, T_2 and off-resonance frequencies are 340 ms, 50 ms and −4 Hz (**c**) and 340 ms, 50 ms, −13 Hz (**d**). The plots are normalized to their maximum value.

off-resonance simultaneously, as shown in Fig. 3b. Because these errors are incoherent with the expected MRF signals, they are largely ignored by the following processing steps. Figure 3c–f shows that high quality estimates of the magnetic resonance parameters are generated even with this significant level of undersampling. White-matter, grey-matter and cerebrospinal-fluid regions were then selected from the resultant maps. The mean T_1 and T_2 values obtained from each region are listed in Table 1 and are within the range of previously reported literature values[29–32]. The shortened T_2 value in CSF is probably due to out-of-plane flow in this two-dimensional experiment. A similar effect can also be observed in conventional T_2 mapping techniques[33]. We also note that the roughly −220 Hz chemical shift of fat protons is clearly visualized in the off-resonance map.

Motion error tolerance in MRF

Because motion is one of the most common sources of error in an MRI scan, a motion-corrupted scan was performed using the accelerated MRF acquisition described in the previous section. The subject was instructed to randomly move his head for the last 3 s of a total 15-s scan. Supplementary Video 3 shows the random motion as well as severe undersampling artefacts in the reconstructed images. Figure 4 compares the quantitative maps from the data with and without the motion-corrupted data. The maps acquired during motion show almost no sensitivity to the motion, and show nearly the same quality and anatomy as the maps from the motion-free data, thus indicating that the signal changes resulting from motion were uncorrelated with the evolutions included in the dictionary, and were largely ignored by the pattern recognition algorithm.

Accuracy and efficiency of MRF

The accuracy and efficiency of the MRF acquisitions were compared with alternative mapping strategies, namely, standard spin-echo sequences[34] as well as modern rapid combined T_1 and T_2 mapping methods DESPOT1 and DESPOT2 (driven equilibrium single pulse observation of T_1 and T_2, respectively)[30] using manufactured agar phantoms. Figure 5a compares the phantom T_1 and T_2 values from these methods. The concordance coefficient correlations for T_1 and T_2 between MRF and spin-echo sequence were 0.988 and 0.974, respectively. The concordance coefficient correlations for T_1 and T_2 between DESPOT and spin-echo sequence were 0.956 and 0.914, respectively.

The high concordance correlation coefficients indicate that both methods are in good agreement with standard spin-echo measurements, and that MRF shows a better accuracy than DESPOT1 and DESPOT2.

The theoretical comparison of the efficiency from various mapping methods has been presented[35,36] and is based on a measure of precision per square root of scan time. In those publications, DESPOT1 and DESPOT2 were shown to have greater efficiency than all previously known conventional and accelerated mapping strategies[36]. As can be seen in Fig. 5b, MRF outperforms both DESPOT1 and DESPOT2 by an average factor of 1.87 and 1.85, respectively. For example, at a T_1 of ~1,280 ms, MRF shows an average efficiency for estimation of T_1 of 24.2, whereas DESPOT1 has an average efficiency of 10.89. This means that for this T_1 value, MRF achieves a precision of ±15.2 ms (or 1.2%) in 12 s of scan time, whereas the precision in DESPOT1 would be ±33.9 ms (or 2.6%) for the same scan time. The DESPOT methods apparently display higher efficiency from the single phantom, with T_1 of 360 ms and T_2 of 53 ms. However, in this one particular phantom, DESPOT overestimated the values of T_1 and T_2 by 23% and 42%, respectively, compared to the standard values, as can be seen in Fig. 5a, thus causing an erroneous increase in the apparent efficiency. Note that these efficiency estimates do not include the waiting times between the acquisition of the different sub-sequences in DESPOT, nor do they include the time required to reach steady state during each acquisition, and thus should be viewed as conservative estimates of the performance of MRF when compared to DESPOT1 or DESPOT2.

Because there is no steady state in the signal evolution from MRF, new information will be continuously added by longer acquisitions. Figure 5c and d illustrates the changes of mean and standard deviation as different acquisition times were used to quantify T_1 and T_2, with a clear trend towards lower error at longer acquisition times. Thus one can select a trade-off between precision and scan time.

Discussion and conclusions

The MRF concept presented here is a new approach to magnetic resonance and provides many opportunities to extend such measurements beyond their current limits. This originates from the unique pulse sequence design concept in MRF, where the goal is to generate unique signal evolutions that can be matched to theoretical signal evolutions and subsequently yield underlying quantitative information
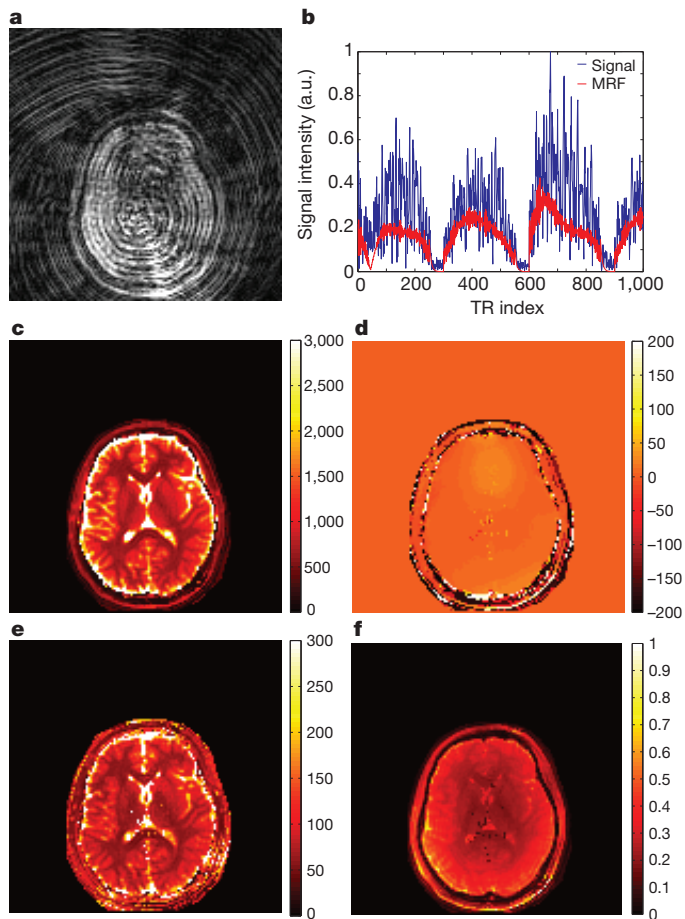
Figure 3 | MRF results from highly undersampled data. a, An image at the 5th repetition time out of 1,000 was reconstructed from only one spiral readout, demonstrating the significant errors from undersampling. **b,** One example of acquired single evolution and its match to the dictionary. Note the significant interference resulting from the undersampling. a.u., arbitrary units. **c–f,** The reconstructed parameter maps show a near complete rejection of these errors based solely on the incoherence between the underlying MRF signals and the undersampling errors; **c,** T_1 (colour scale, milliseconds); **d,** off-resonance frequency (colour scale, hertz); **e,** T_2 (colour scale, milliseconds); and **f,** proton density (M_0) (normalized colour scale). These data required 12.3 s to acquire.
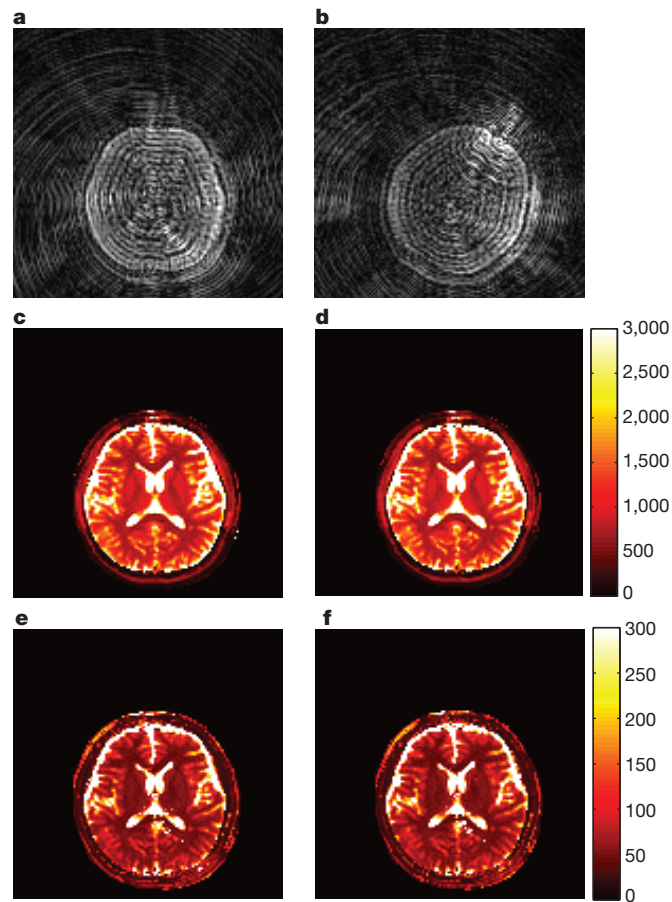

Figure 4 | Demonstration of error tolerance in the presence of motion. a, b, Reconstructed images acquired at the 12th second (**a**) and at the 15th second (**b**) demonstrate the large shift in the head position. **c–f,** The resulting MRF maps are nearly identical, demonstrating a rejection of both undersampling and motion errors that are uncorrelated with the expected signal evolution. **c, d,** T_1 (colour scale, milliseconds); **e, f,** T_2 (colour scale, milliseconds); **c** and **e** are from the first 12 s that has no motion, **d** and **f** are from entire 15 s that includes the motion.

about the material, tissue or pathology of interest. Because there is no *a priori* requirement on the shape of the signal evolution curves, there are more degrees of freedom in designing an MRF acquisition, where parameters such as repetition time, echo time, radio frequency pulses and sampling trajectories (among others) can be varied together to produce the simultaneous sensitivity to numerous tissue properties. The ability to analyse oscillating signals in MRF also provides the opportunity to use larger fractions of the available magnetization than methods that rely on a steady-state signal, which is a significant factor contributing to the higher efficiency in MRF. In addition, the oscillatory signal in MRF allows one to sample more informative points along a longer signal evolution as compared to conventional methods which always reach a steady state level after some finite amount of time. Specifically, our initial results here demonstrate that the efficiency of MRF is approximately 1.8 times higher than the DESPOT methods, which were previously the most efficient methods for the measurement of relaxation parameters. Thus the direct prediction of the oscillating, incoherent signal evolutions through the Bloch simulation provides us the potential to obtain new quantitative information that is impractical today because of the prohibitively long scan times required, especially in biological samples and patients.

As demonstrated by the results shown here, MRF has the potential to significantly reduce the effects of errors during acquisition through its basis in pattern recognition. Acquisition errors may globally reduce the probability of a match of an observed signal to any given fingerprint, but as long as the errors do not cause another fingerprint to become the most likely match, the correct quantitative identification will still be made. Ideally, the sequence pattern will be designed so that the various fingerprints from different tissues and materials are as independent as possible, thus ensuring this robustness against motion and other practical errors.

Commercial magnetic resonance scanners include methods to minimize the effects of unavoidable system imperfections. However, these inaccuracies are becoming increasingly important as magnetic resonance technology is pushed to its limits, such as the use of very high magnetic fields or physically larger systems. MRF provides a route to model and account for system imperfections, such as inhomogeneities in both the static magnetic field (B_0) and the

Table 1 | *In vivo* data

	T_1 (ms)	T_2 (ms)
White matter (this work)	685 ± 33	65 ± 4
White matter (previously reported)	608–756	54–81
Grey matter (this work)	1,180 ± 104	97 ± 5.9
Grey matter (previously reported)	998–1,304	78–98
Cerebrospinal fluid (this work)	4,880 ± 379	550 ± 251
Cerebrospinal fluid (previously reported)	4,103–5,400	1,800–2.460

Shown are comparisons of MRF results and reference values[29–32] in different brain regions.
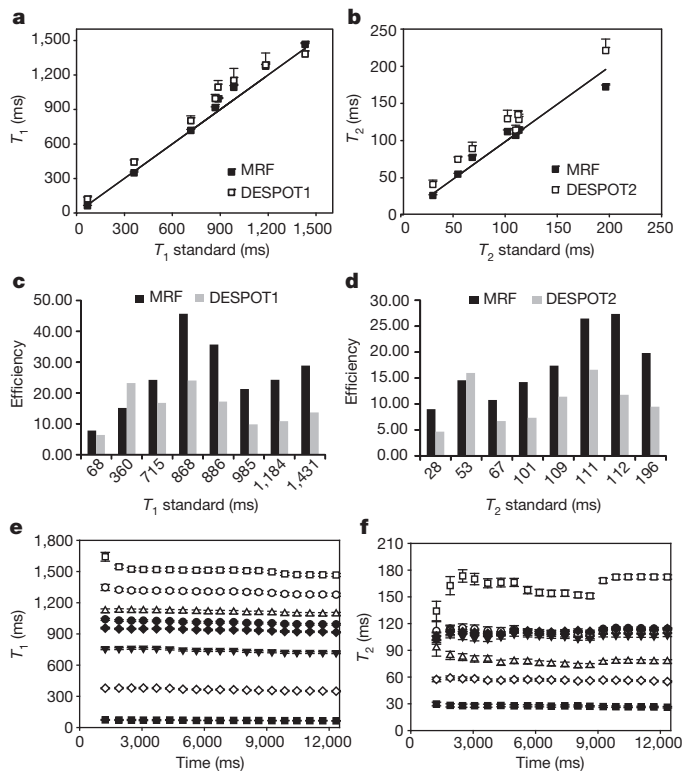
Figure 5 | Accuracy, efficiency and error estimation for MRF and DESPOT.
a, **b**, The T_1 and T_2 values retrieved from MRF from eight phantoms are
compared with those acquired from DESPOT1 (**a**), DESPOT2 (**b**) and a
standard spin-echo sequence. **c**, **d**, The efficiency of MRF compared to
DESPOT1 (**c**) and DESPOT2 (**d**) at different T_1 and T_2 values; efficiency is
assessed as precision per (acquisition time)$^{1/2}$. MRF has an average of 1.87 and
1.85 times higher efficiency than DESPOT1 and DESPOT2, respectively.
e, **f**, Obtained values of T_1 (**e**) and T_2 (**f**) as a function of acquisition time. Data in
a–d show mean ± s.d. of the results over a 25-pixel region in the centre of each
phantom, and are smaller than the symbols for most MRF results.

applied radio frequency field (B_1), by adding these parameters into the
dictionary simulation. Because both MRF and DESPOT2 are based on
a bSSFP sequence, which is known to be sensitive to field inhomo-
geneities[30,37], Supplementary Fig. 2 compares the T_2 maps acquired
from MRF and DESPOT2 from an *in vivo* scan. Because off-resonance
is not taken into account in the DESPOT2 model, the T_2 map from
DESPOT2 shows areas of signal voids resulting from susceptibility
effects at the air–tissue interfaces. MRF naturally incorporates these
effects into the fingerprints, and thus the maps generated by MRF do
not show these errors. Thus MRF could, for example, provide higher
quality results using the current generation of magnetic resonance
scanners. Alternatively, MRF could also allow the design of lower cost
magnetic resonance scanners that can provide the same quality as
today's high end systems through application of MRF models.

Because of its ability to provide quantitative results across many
parameters simultaneously, MRF could lead to the direct identi-
fication of a material, tissue or pathology solely on the basis of its
fingerprint. For example, many cancer cells show changes in multiple
magnetic resonance parameters (for example, T_1, T_2 and self-diffusion
tensor), a combination (though no single parameter) of which could
potentially characterize them as different from all surrounding normal
tissue types, and thus potentially separable. In an ideal situation, each
given material, tissue or pathology would have its own signal evolution
which would be orthogonal to all other signal evolutions. The MRF
concept also implies that completely different acquisition schemes
are possible in cases where one is only interested in the presence or
absence of a particular material or disease state. For example, one
could do a very rapid MRF scan of a bulk area of material or tissue

and compare the measured signal evolutions against the set of known
states of interest. This measurement could either indicate the presence
of the material or disease of interest, or indicate its absence within a
margin of error. This feature could result in very rapid and accurate
screening procedures. In particular, this feature may help to relax
the required spatial resolution of an MRI examination, thus increasing
the speed, and potentially reducing the cost, of such an examination.
A preliminary example of this kind of visualization is shown in
Supplementary Information Section 3. Using the MRF concept, the
operation of the magnetic resonance unit will also be greatly simpli-
fied, because the 'all in one' scan concept of MRF has the potential to
reduce the dozens of parameters currently presented to the magnetic
resonance operator to a simple 'scan' button.

It is important to note that the proof-of-principle implementation
of MRF shown here is but one of the many possibilities that could be
used for this technique, and both the sequence design/implementa-
tion and post-processing methods will continue to be a significant
open area of research, just as sequence design has advanced over the
decades since the conventional methods have been introduced. Other,
more advanced pattern recognition algorithms[38–42] will probably
improve the performance of MRF. For spatially encoded MRI appli-
cations, the parameters retrieved from MRF are far fewer than the
number of pixels in the images, and because the signals generated
are largely incoherent, MRF has the additional potential to be highly
accelerated through combination with other compressed sensing
methods for accelerated spatial encoding, in addition to the now stan-
dard parallel imaging methods[43–45], neither of which were included
here. Any of these methods would reduce the undersampling errors
seeing in Fig. 3a even before the pattern recognition step, which
should result in higher quality results. We have recently published
data indicating that we can achieve a reduction in imaging time of
about ten times for a two-dimensional slice using parallel imaging
alone[43,45,46]. Also, it should be noted that the proof-of-principle results
shown here only take advantage of two spatial dimensions for under-
sampling, whereas it is well known that taking full advantage of
undersampling in all three spatial dimensions gives higher perform-
ance than a two-dimensional acquisition owing to the reduced power
of the resulting errors at any given undersampling factor[47]. Thus a
combination of an optimized three-dimensional MRF pulse sequence
with parallel imaging and more advanced pattern matching algo-
rithms will allow realization MRF in very short scan times.

METHODS SUMMARY

Sequence design. After an initial inversion pulse, the sequence pattern shown in
Fig. 1c used a pseudorandomized series (Perlin noise[48]) of flip angle and a random
repetition time from 10.5 to 14 ms. The flip angle pattern in Fig. 1d contained
repeating sinusoidal curves with a period of 250 acquisitions and alternating
maximum flip angles. The repetition time was a Perlin noise pattern. The radio
frequency phase for both of the patterns alternated between 0 and 180° on
successive radio frequency pulses. The variable density spiral-out trajectory was
designed using minimum-time gradient design[49].

Dictionary design. A total of 563,784 signal time courses, each with 1,000 time
points, with different sets of characteristic parameters (T_1, T_2 and off-resonance)
were simulated for the dictionary. One dictionary entry was selected for each
measured pixel location using template matching. In this case, the vector dot-
product was calculated between the measured time course and all dictionary
entries using complex data for both. The dictionary entry with the highest dot-
product was then selected as most likely to represent the true signal evolution. The
M_0 value is then the multiplicative constant derived by fitting the acquired data to
this dictionary entry.

Data acquisition. All data were acquired on a 1.5-T whole body scanner (Espree,
Siemens Healthcare) with a standard 32-channel head receiver coil. Images from
each acquisition block were reconstructed separately using non-uniform Fourier
transform[50]. The resultant time series of images was used to determine the value
for the parameters (T_1, T_2, M_0 and off-resonance) as described above.

Statistical analysis. Quantitative estimates of the errors and efficiencies of MRF,
DESPOT1 and DESPOT2 were calculated pixel-wise using a bootstrapped Monte
Carlo method[51]. The means and standard deviations of T_1 and T_2 along the 50

repetitions were calculated, and averaged within a square (5 pixel × 5 pixel) region of interest for each phantom. The concordance correlation coefficients and efficiency were calculated as in refs 30 and 52.

Full Methods and any associated references are available in the online version of the paper.

1. Bartzokis, G. et al. In vivo evaluation of brain iron in Alzheimer disease using magnetic resonance imaging. Arch. Gen. Psychiatry **57,** 47–53 (2000). .
2. Larsson, H. B. et al. Assessment of demyelination, edema, and gliosis by in vivo determination of T1 and T2 in the brain of patients with acute attack of multiple sclerosis. Magn. Reson. Med. **11,** 337–348 (1989).
3. Pitkänen, A. et al. Severity of hippocampal atrophy correlates with the prolongation of MRI T2 relaxation time in temporal lobe epilepsy but not in Alzheimer's disease. Neurology **46,** 1724–1730 (1996).
4. Williamson, P. et al. Frontal, temporal, and striatal proton relaxation times in schizophrenic patients and normal comparison subjects. Am. J. Psychiatry **149,** 549–551 (1992).
5. Warntjes, J. B. Dahlqvist, O. & Lundberg, P. Novel method for rapid, simultaneous T1, T*2, and proton density quantification. Magn. Reson. Med. **57,** 528–537 (2007).
6. Warntjes, J. B. Leinhard, O. D., West, J. & Lundberg, P. Rapid magnetic resonance quantification on the brain: optimization for clinical usage. Magn. Reson. Med. **60,** 320–329 (2008).
7. Schmitt, P. et al. Inversion recovery TrueFISP: quantification of T1, T2, and spin density. Magn. Reson. Med. **51,** 661–667 (2004).
8. Ehses, P. et al. IR TrueFISP with a golden-ratio-based radial readout: fast quantification of T1, T2, and proton density. Magn. Reson. Med. **69,** 71–81 (2013).
9. Donoho, D. L. Compressed sensing. IEEE Trans. Inform. Theory **52,** 1289–1306 (2006).
10. Candes, E. J. & Tao, T. Near-optimal signal recovery from random projections: universal encoding strategies? IEEE Trans. Inform. Theory **52,** 5406–5425 (2006).
11. Lustig, M., Donoho, D. L. & Pauly, J. M. Sparse MRI: the application of compressed sensing for rapid MR imaging. Magn. Reson. Med. **58,** 1182–1195 (2007).
12. Bilgic, B., Goyal, V. K. & Adalsteinsson, E. Multi-contrast reconstruction with Bayesian compressed sensing. Magn. Reson. Med. **66,** 1601–1615 (2011).
13. Smith, D. S. et al. Robustness of quantitative compressive sensing MRI: the effect of random undersampling patterns on derived parameters for DCE- and DSC-MRI. IEEE Trans. Med. Imaging **31,** 504–511 (2012).
14. Deshpande, V. S., Chung, Y.-C., Zhang, Q., Shea, S. M. & Li, D. Reduction of transient signal oscillations in True-FISP using a linear flip angle series magnetization preparation. Magn. Reson. Med. **49,** 151–157 (2003).
15. Çukur, T. Multiple repetition time balanced steady-state free precession imaging. Magn. Reson. Med. **62,** 193–204 (2009).
16. Nayak, K. & Lee, H. Wideband SSFP: alternating repetition time balanced steady state free precession with increased band spacing. Magn. Reson. Med. **58,** 931–938 (2007).
17. Lee, K., Lee, H. & Hennig, J. Use of simulated annealing for the design of multiple repetition time balanced steady-state free precession imaging. Magn. Reson. Med. **68,** 220–226 (2012).
18. Ernst, R. R. Magnetic resonance with stochastic excitation. J. Magn. Reson. **3,** 10–27 (1970).
19. Scheffler, K. & Hennig, J. Frequency resolved single-shot MR imaging using stochastic k-space trajectories. Magn. Reson. Med. **35,** 569–576 (1996).
20. Haldar, J. P., Hernando, D. & Liang, Z.-P. Compressed-sensing MRI with random encoding. IEEE Trans. Med. Imaging **30,** 893–903 (2011).
21. Doneva, M. et al. Compressed sensing reconstruction for magnetic resonance parameter mapping. Magn. Reson. Med. **64,** 1114–1120 (2010).
22. Stoecker, T., Vahedipour, K., Pracht, E., Brenner, D. & Shah, N. J. in Proc. 19th Scientific Meeting International Society for Magnetic Resonance in Medicine 381 (Int. Soc. Magn. Reson. Med., 2011).
23. Davenport, M. A., Wakin, M. B. & Baraniuk, R. G. The Compressive Matched Filter (Tech. Rep. TREE 0610, Rice University, 2006).
24. Tropp, J. A. & Gilbert, A. C. Signal recovery from random measurements via orthogonal matching pursuit. IEEE Trans. Inform. Theory **53,** 4655–4666 (2007).
25. Schmitt, P. et al. A simple geometrical description of the TrueFISP ideal transient and steady-state signal. Magn. Reson. Med. **55,** 177–186 (2006).
26. Lee, J. H., Hargreaves, B. A., Hu, B. S. & Nishimura, D. G. Fast 3D imaging using variable-density spiral trajectories with applications to limb perfusion. Magn. Reson. Med. **50,** 1276–1285 (2003).
27. Marseille, G., De Beer, R., Fuderer, M., Mehlkopf, A. & Van Ormondt, D. Nonuniform phase-encode distributions for MRI scan time reduction. J. Magn. Reson. B. **111,** 70–75 (1996).
28. Tsai, C. M. & Nishimura, D. G. Reduced aliasing artifacts using variable-density K-space sampling trajectories. Magn. Reson. Med. **43,** 452–458 (2000).
29. Vymazal, J. et al. T1 and T2 in the brain of healthy subjects, patients with Parkinson disease, and patients with multiple system atrophy: relation to iron content. Radiology **211,** 489–495 (1999).
30. Deoni, S. C. L., Peters, T. M. & Rutt, B. K. High-resolution T1 and T2 mapping of the brain in a clinically acceptable time with DESPOT1 and DESPOT2. Magn. Reson. Med. **53,** 237–241 (2005).
31. Whittall, K. P. et al. In vivo measurement of T2 distributions and water contents in normal human brain. Magn. Reson. Med. **37,** 34–43 (1997).
32. Poon, C. S. & Henkelman, R. M. Practical T2 quantitation for clinical applications. J. Magn. Reson. Imaging **2,** 541–553 (1992).
33. Haacke, E. M., Brown, R. W., Thompson, M. R. & Venkatesan, R. Magnetic Resonance Imaging: Physical Principles and Sequence Design 669–675 (Wiley & Sons, 1999).
34. Hahn, E. L. Spin echoes. Phys. Rev. **80,** 580–594 (1950).
35. Crawley, A. P. & Henkelman, R. M. A Comparison of one-shot and recovery methods in T1 imaging. Magn. Reson. Med. **7,** 23–34 (1988).
36. Deoni, S. C. L., Rutt, B. K. & Peters, T. M. Rapid combined T1 and T2 mapping using gradient recalled acquisition in the steady state. Magn. Reson. Med. **49,** 515–526 (2003).
37. Scheffler, K. & Lehnhardt, S. Principles and applications of balanced SSFP techniques. Eur. Radiol. **13,** 2409–2418 (2003).
38. Needell, D. & Tropp, J. A. Cosamp: iterative signal recovery from incomplete and inaccurate samples. Appl. Comput. Harmon. Anal. **26,** 301–321 (2009).
39. Goldstein, T. & Osher, S. The split Bregman method for L1-regularized problems. SIAM J. Imaging Sci. **2,** 323–343 (2009).
40. Chartrand, R. & Yin, W. in Proc. ICASSP 2008 IEEE International Conference 3869–3872 (IEEE, 2008).
41. Wright, J., Yang, A. Y., Ganesh, A., Sastry, S. S. & Ma, Y. Robust face recognition via sparse representation. IEEE Trans. Pattern Anal. Mach. Intell. **31,** 210–227 (2009).
42. Turk, M. & Pentland, A. Eigenfaces for recognition. J. Cogn. Neurosci. **3,** 71–86 (1991).
43. Griswold, M. A. et al. Generalized autocalibrating partially parallel acquisitions (GRAPPA). Magn. Reson. Med. **47,** 1202–1210 (2002).
44. Pruessmann, K. P. et al. SENSE: sensitivity encoding for fast MRI. Magn. Reson. Med. **42,** 952–962 (1999).
45. Seiberlich, N., Ehses, P., Duerk, J., Gilkeson, R. & Griswold, M. A. Improved radial GRAPPA calibration for real-time free-breathing cardiac imaging. Magn. Reson. Med. **65,** 492–505 (2011).
46. Heidemann, R. M. et al. Direct parallel image reconstructions for spiral trajectories using GRAPPA. Magn. Reson. Med. **56,** 317–326 (2006).
47. Barger, A. V., Block, W. F., Toropov, Y., Grist, T. M. & Mistretta, C. A. Time-resolved contrast-enhanced imaging with isotropic resolution and broad coverage using an undersampled 3D projection trajectory. Magn. Reson. Med. **48,** 297–305 (2002).
48. Perlin, K. An image synthesizer. Comput. Graphics **19,** 287–296 (1985).
49. Hargreaves, B. A., Nishimura, D. G. & Conolly, S. M. Time-optimal multidimensional gradient waveform design for rapid imaging. Magn. Reson. Med. **51,** 81–92 (2004).
50. Fessler, J. A. & Sutton, B. P. Nonuniform fast Fourier transforms using min-max interpolation. IEEE Trans. Signal Process. **51,** 560–574 (2003).
51. Riffe, M. J., Blaimer, M., Barkauskas, K. J., Duerk, J. L. & Griswold, M. A. in Proc. 15th Scientific Meeting, International Society for Magnetic Resonance in Medicine 1879 (Int. Soc. Magn. Reson. Med, 2007).
52. Lin, L. I.-K. A concordance correlation coefficient to evaluate reproducibility. Biometrics **45,** 255–268 (1989).

Author Contributions D.M., concept development, technical implementation, data collection and analysis, manuscript development and editing; V.G., concept development, manuscript development and editing; N.S., concept development, manuscript development and editing; K.L., concept development, technical implementation, manuscript development and editing; J.L.S., concept development, manuscript development and editing; J.L.D., concept development, manuscript development and editing; M.A.G., concept development, data collection and analysis, manuscript development and editing.

Author Information Reprints and permissions information is available at www.nature.com/reprints. The authors declare competing financial interests: details are available in the online version of the paper. Readers are welcome to comment on the online version of the paper. Correspondence and requests for materials should be addressed to M.A.G. (mark.griswold@case.edu).

METHODS

Sequence design. After an initial inversion pulse, the first sequence pattern shown in Fig. 1c used a pseudorandomized series (Perlin noise[48]) of flip angle and a random repetition time between 10.5 ms and 14 ms based on a uniform random number generator. A linear ramp was added to the flip angle train since we have seen that this can increase differential sensitivity to both T_1 and T_2.

The second flip angle pattern in Fig. 1d used a series of repeating sinusoidal curves with a period of 250 repetition times and alternating maximum flip angles. In the odd periods, the flip angle (FA) is calculated as $FA_t = 10 + \sin\left(\frac{2\pi}{500} t\right) \times 50 + \mathrm{random}(5)$, where t is from 1 to 250, and random(5) is a function to generate uniformly distributed values with a standard deviation of 5. In the even periods, we divide the previous period's flip angle by 2. A 600 ms delay was added between each of the periods to allow for both differential magnetization recovery according to T_1 and differential signal decay according to T_2. In this case, the repetition time was a Perlin noise pattern. The radio frequency phase for both of the patterns in Fig. 1 alternated between 0 and 180° on successive pulses.

The variable density spiral-out trajectory was designed to have 5.8 ms readout time in each repetition time and to have zero and first moment gradient compensation using minimum-time gradient design[49]. (The code used for this design is available at http://www-mrsrl.stanford.edu/~brian/mintgrad/). This trajectory required one interleaf to sample the inner 10×10 region, while 48 interleaves were required to fully sample the outer portions of k-space. During acquisition, the spiral trajectory rotated 7.5° from one time point to the next, so that each time point had a slightly different spatial encoding.

Dictionary design. The dictionary used in the matching algorithm was simulated using MATLAB (The MathWorks). Signal time courses with different sets of characteristic parameters (T_1, T_2 and off-resonance) were simulated. The ranges of T_1 and T_2 for the *in vivo* study were chosen according to the typical physiological limits of tissues in the brain: T_1 values were taken to be between 100 and 5,000 ms (in increments of 20 ms below a T_1 of 2,000 ms and in an increment of 300 ms above). The T_2 values included the range between 20 and 3,000 ms (with an increment of 5 ms below a T_2 of 100 ms, an increment of 10 ms between 100 ms and 200 ms, and an increment of 200 ms above a T_2 of 200 ms). Since magnetic resonance is sensitive to parts per million (p.p.m.) level deviations in the B_0 field, different off-resonance frequencies (1 Hz increment between ± 40 Hz, 2 Hz between ± 40 to ± 80 Hz, 10 Hz between ± 90 to ± 250 Hz, and 20 Hz between ± 270 to ± 400 Hz) were simulated for each combination of T_1 and T_2 parameters to incorporate the effects of signal evolutions in different B_0 fields. A total of 563,784 dictionary entries, each with 1,000 time points, were generated in 399 s on a standard desktop computer. One dictionary entry was selected for each measured pixel location using template matching. In this case, the vector dot-product was calculated between the measured time course and all dictionary entries (appropriately normalized to each having the same sum squared magnitude) using the complex data for both. The dictionary entry with the highest dot-product was then selected as most likely to represent the true signal evolution. The proton density (M_0) of each pixel was calculated as the scaling factor between the measured signal and the simulated time course from the dictionary. For this experiment, four parameters were retrieved simultaneously from each of the 128×128 pixels using MRF. This calculation required about 3 min on a standard desktop computer.

Data acquisition. All MRI and MRF data were acquired on a 1.5 T whole body scanner (Siemens Espree, Siemens Healthcare) with a 32 channel head receiver coil (Siemens Healthcare). A square field of view of 300 mm × 300 mm was covered with a matrix of 128 × 128 pixels. The slice thickness was 5 mm. Images from each acquisition block were reconstructed separately using non-uniform Fourier transform (NUFFT)[50]. The resultant time series of images was

used to determine the value for the parameters (T_1, T_2, M_0 and off-resonance) as described above.

In vivo experiments were performed with IRB guidelines, including written informed consent. For the fully sampled spiral acquisition shown in Supplementary Video 1, 48 repetitions were acquired, each with a different interleaf of the total acquisition. A recovery time of 5 s was used in between various acquisitions and this was taken into account in the simulated dictionary.

For the phantom study shown in Figs 2 and 4, eight cylindrical phantoms were constructed with varying concentrations of $GdCl_3$ (Aldrich) and agarose (Sigma) to yield different T_1 and T_2 values ranging from 67 to 1,700 ms and 30 to 200 ms, respectively. Standard spin echo sequences were used to quantify T_1 and T_2 separately (T_1 quantification: 13 repetition times (TRs) ranging from 50 to 5,000 ms, echo time TE = 8.5 ms, total acquisition time = 33.4 min; T_2 quantification: spin echo sequences with TEs = [15, 30, 45, 60, 90, 150, 200, 300, 400] ms, TR = 10,000 ms, total acquisition time = 3.2 h). T_1 values were calculated pixel-wise using a standard three-parameter nonlinear least squares fitting routine to solve the equation: $S(TR) = a + b e^{TR/T1}$. T_2 values were determined in a pixel-wise fashion using a two-parameter nonlinear least squares fitting routine to solve the equation $S(TE) = a e^{-TE/T2}$, DESPOT1 and DESPOT2 sequences using a fully sampled spiral readout were implemented based on the acquisition values from ref. 30: DESPOT1: FA: 4° and 15°, TR: 13.6 ms, DESPOT2: FA: 15° and 55°, TR = 10.8 ms. The T_1 and T_2 values were calculated from the equations provided in ref. 30. A 20 s waiting period was used in between the different acquisitions. The initial 10 s of data acquisition was not used in order to ensure that the signal was in steady-state for each of the DESPOT acquisitions. In the following analysis of efficiency, only the pure time of data acquisition for the steady-state DESPOT images is used. For DESPOT1 this was 1.27 s and for DESPOT2 it was 2.29 s (which includes the time for the required DESPOT1 acquisition).

Statistical analysis. Quantitative estimates of the errors and efficiencies of MRF, DESPOT1 and DESPOT2 were calculated pixel-wise using a bootstrapped Monte Carlo method[51]. Two sets of raw data were acquired for each sequence: the encoded signal and a separate acquisition that only contained noise. Fifty reconstructions were then calculated by randomly resampling the acquired noise and adding it to the raw data before reconstruction and quantification. The means and standard deviations of T_1 and T_2 along the 50 repetitions were calculated, and both were averaged within a 5 pixel × 5 pixel square region of interest for each phantom. The concordance correlation coefficients (ρ_c) were calculated using the equation[52]:

$$\rho_c = \frac{2S_{12}}{S_1^2 + S_2^2 + (\overline{Y_2} - \overline{Y_1})^2}$$

where Y_1 and Y_2 denotes the T_1 or T_2 values from two different methods, n is the number of phantoms, $\overline{Y_j} = \frac{1}{n}\sum_{i=1}^{n} Y_{ij}$, $S_j^2 = \frac{1}{n}\sum_{i=1}^{n}(Y_{ij} - \overline{Y_j})^2$, $j = 1,2$ and $S_{12} = \frac{1}{n}\sum_{i=1}^{n}(Y_{i1} - \overline{Y_1})(Y_{i2} - \overline{Y_2})$.

The efficiency of the methods was calculated using:

$$\text{Efficiency} = \frac{T_n NR}{\sqrt{T_{seq}}}, \quad n = 1,2$$

where $T_n NR$ is the T_1 or T_2 to noise ratio (defined as the T_1 or T_2 value divided by the estimated error). T_{seq} is the total acquisition time for MRF, and the relevant acquisition times for DESPOT1 and DESPOT2 (where the waiting times required for the approach to steady state and the time between each of the DESPOT1 and DESPOT2 scans to allow for complete recovery of magnetization were ignored).